NONLINEAR CREEP OF CONCRETE: THE DRIVING ROLE OF VISCOELASTICITY AND CRACKING-INDUCED DAMAGE

RODRIGO DÍAZ FLORES[*], CHRISTIAN HELLMICH[*] AND BERNHARD PICHLER[*]

[*] Technische Universität Wien, Institute of Mechanics of Materials and Structures
Karlsplatz 13, 1040 Vienna, Austria
e-mail: rodrigo.diaz@tuwien.ac.at

Key words: Nonlinear creep, viscous interfaces, nonlinear viscoelasticity, microcracking, damage mechanics

Abstract: Creep of concrete refers to the progressive increase of deformation of a representative material volume subjected to a sustained stress. At low ratios between applied stress and material strength, an increase of the stress relates to an approximately linear increase of the deformation. Nonlinearities occur once the stress exceeds some 40% of the strength. In this work, the origins of such nonlinearities are explored, explicitly separating the contributions from viscoelastic processes and damage due to cracking. A multilevel uniaxial compressive creep test on a mature concrete [1] is re-analyzed. Additionally to documenting the prescribed loading and to measuring the strains, the acoustic emission technique was used to monitor the creation of microcracks. These data were used as input to formulate an analytical model as follows. The reported strength was related to the hydration degree of the material via a validated multiscale model. The obtained hydration degree, together with the mix design, served as input for quantifying linear, nonaging, basic creep properties of uncracked concrete by means of another well-validated multiscale model for creep of cementitious materials under saturated conditions. The obtained creep function was then extended to account for (i) different levels of time-invariant relative humidity (constant moisture during creep testing), by means of a creep reduction factor, (ii) nonlinear viscoelastic processes, by means of the affinity concept [2], and (iii) diffuse microcracking, by means of a micromechanics-motivated damage factor which relates the creation of microcracks to a proportional increase in the compliance of concrete. In [5], it was shown that cracks created during both quasi-static load application and sustained loading have an important influence on the deformation behavior of concrete. Herein, further experiments are analyzed. This confirms that nonlinear viscoelastic phenomena govern the creep behavior at medium stress levels, while cracking-induced damage dominates the behavior at high stress levels.

1 INTRODUCTION

Nonlinear creep of concrete and its microstructural origin is the subject of an ongoing scientific debate. Common modelling strategies include (i) the use of the micro-prestress-solidification theory [3,4], considering couplings between creep, drying, and cracking; and (ii) the use of the affinity concept [2], stating that nonlinear creep is affine to linear creep through an affinity parameter which is a function of the stress-to-strength ratio. The former models tend to be more general but are also quite complex and require the calibration of many different parameters. The latter model is much simpler but leaves the mechanisms behind nonlinear creep unclarified.

Recently [5], a model was developed for nonlinear creep of concrete based on the experimental data from Rossi et al. [1], where the influences of aging [6], drying [7], and

temperature changes [8] are negligible. The model suggests, through a comparison between micromechanical and rheological models [9,10], that nonlinear creep occurs due the combination of (i) nonlinear viscoelastic phenomena, explained through the affinity concept, and (ii) diffuse microcracking-induced damage, modelled through a newly introduced damage factor that relates the creation of microcracks to a proportional increase in the compliance of concrete.

The present contribution is organized as follows. Section 2 presents the multistage nonlinear creep test by the Rossi et al. [1]. Section 3 refers to micromechanics-based damage modelling, accounting for different types of crack networks. Section 4 contains the application of the damage approach to multiscale nonlinear creep modelling. Section 5 is devoted to laws for the evolution of diffuse microcracking during load application and during sustained loading, respectively [5]. In Section 6, the model is newly employed for the analysis of two sets of linear and nonlinear creep tests on CEM I and CEM II concretes. Finally, conclusions are presented in Section 7.

2 MULTILEVEL UNIAXIAL COMPRESSION CREEP TEST AT LARGE STRESS LEVELS

Rossi et al. [1] used the technique of acoustic emissions to analyze a multilevel basic nonlinear creep test performed in five stages. While subjecting a slender concrete cylinder (diameter = 16 cm, height = 100 cm) to uniaxial compression, measurements of the prescribed stress and of the induced strain were taken, and the number of acoustic events was recorded. Herein, the first three load stages are analyzed, given that strain *and* acoustic events can both be identified as a function of time. As regards the latter two stages, [1] only provides the number of acoustic events as a function of the strain, but not as a function of time.

The basic creep tests were performed on concrete made up of CEM I 52.5 N, a water-to-cement mass ratio of 0.54, a volume fraction of cement paste of 0.292, and a volume fraction of sand-lime aggregates of 0.708.

The test was started at a material age of 266 days. The load was first increased to 24.9 MPa, i.e. the stress-to-28-day-strength ratio amounted to some 54%. This was kept constant for 87 days. Then the loading was increased to 27.3 MPa, i.e. the stress-to-28-day-strength ratio amounted to some 59%. This was kept constant for the following 31 days. Thereafter, the loading was increased up to 33.6 MPa, i.e. stress-to-28-day-strength ratio amounted to some 73%. This was kept constant for 7 days, see Figure 1, Figure 2, and Figure 3 for the prescribed levels of stress and the measured values of strain and of the number of acoustic events, respectively.
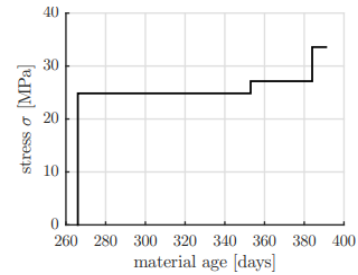
Figure 1: Stress history prescribed during the nonlinear creep test by Rossi et al. [1]; taken from [5].
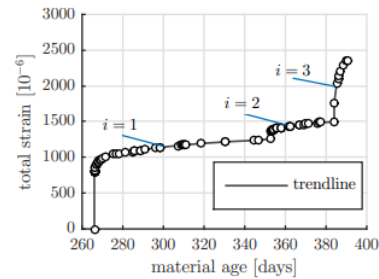
Figure 2: Strain history measured during the nonlinear creep test by Rossi et al. [1]; taken from [5].
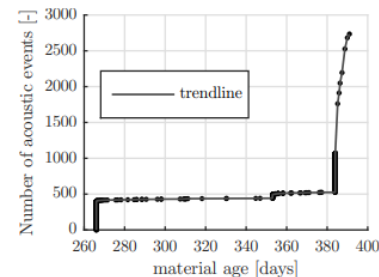
Figure 3: Number of acoustic events measured during the nonlinear creep test by Rossi et al. [1]; taken from [5].

The strength of concrete at the time of loading was uncertain. This motivated a

2

sensitivity analysis, denoted by the index $k = 1, 2, 3$, yielding different hydration degrees associated to each strength [5]. Each hydration degree refers to a different set of mechanical properties (E … elastic modulus, E_c … creep modulus), as follows [5]:

- For $k = 1$, the elastic and creep modulus are $E = 30.9$ GPa and $E_c = 190.2$ GPa.
- For $k = 2$, the elastic and creep modulus are $E = 31.2$ GPa and $E_c = 195.4$ GPa.
- For $k = 3$, the elastic and creep modulus are $E = 31.6$ GPa and $E_c = 200.7$ GPa.

3 MICROMECHANICS-BASED DAMAGE MECHANICS

Concrete damaged by diffuse microcracking is herein modelled as a two-phase material consisting of an uncracked concrete matrix and penny-shaped cracks, see Figure 4. The volume fraction of the cracks is equal to the sum of their volumes, divided by the volume of the Representative Volume Element (RVE) of concrete: $f_{cr} = \frac{4\pi}{3} \omega X$, where X refers to the aspect ratio of the penny-shaped cracks, and ω refers to Budiansky's and O'Connell's [12] crack density parameter, defined as

$$\omega = \frac{Na^3}{V}, \qquad (1)$$

with N as the number of cracks inside a volume V, and a as the characteristic crack radius.
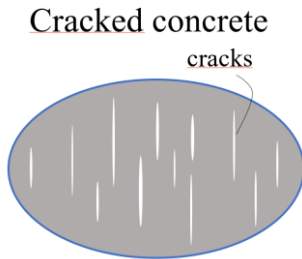
Cracked concrete

Figure 4: Representative Volume Element (RVE) of cracked concrete: penny-shaped cracks embedded in an uncracked concrete matrix (gray); 2D sketch of a 3D RVE; adapted from [5].

Using the Mori-Tanaka scheme [13] for upscaling under consideration of microcrack interaction, the stiffness of damaged concrete is obtained as

$$\mathbb{C}_{dam} = \mathbb{C}_c : \left[\mathbb{I} + \frac{4\pi}{3} \omega \mathbb{T}\right]^{-1}, \qquad (2)$$

where $\mathbb{I}$ refers to the symmetric fourth-order identity tensor, and $\mathbb{T}$ to the $\mathbb{T}$-Tensor introduced by Dormieux and Kondo [14] for cracks with a vanishing aspect ratio. The $\mathbb{T}$-tensor depends on the orientation of the cracks. For parallel cracks, $\mathbb{T} = \mathbb{T}(\theta, \varphi)$, where θ and φ refer to the zenith and azimuth angles of a spherical coordinate system, describing the orientation of the normal to the microcrack plane.

3.1 Isotropic crack orientation

In case of isotropic crack orientations the tensor $\mathbb{T}(\theta, \varphi)$ is to be integrated over all directions, such that

$$\mathbb{T} = \int_{\theta=0}^{\pi} \int_{\varphi=0}^{2\pi} \mathbb{T}(\theta, \varphi) \frac{\sin\theta}{4\pi} \, d\varphi \, d\theta. \qquad (3)$$

Thus, the stiffness of damaged concrete, see Eqs. (1) and (2), is obtained as

$$\frac{1}{E_{dam}} = \frac{1}{E}\left[1 + \omega \frac{16(1-\nu^2)(10-3\nu)}{45(2-\nu)}\right], \qquad (4)$$

and its Poisson's ratio as

$$\nu_{dam} = \frac{45\nu(2-\nu) + 16\,\nu\,\omega\,(1-\nu^2)}{45(2-\nu) + 16\,\omega\,(1-\nu^2)(10-3\nu)}. \qquad (5)$$

These relations are illustrated in Figure 5 (a) and (b), respectively.

(a)
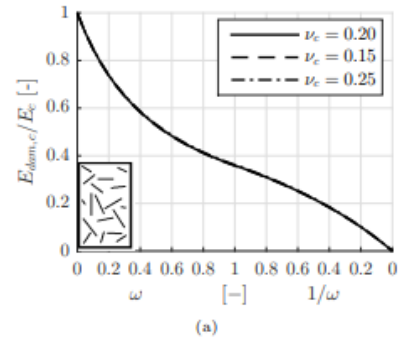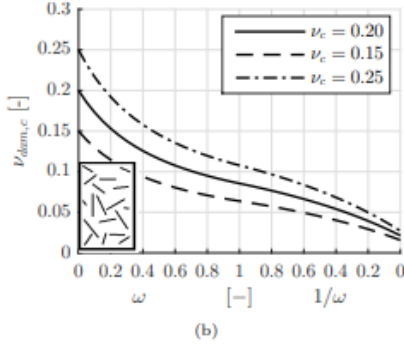
Figure 5: Relations between (a) the elastic modulus, and (b) Poisson's ratio of concrete, as a function of ω for an isotropic crack orientation.

3.2 Axisymmetric crack orientation

Axisymmetric crack orientation around the loading direction have been observed at very high load levels of uniaxial compression experiments, as failure due to axial splitting is triggered. Thus, θ is set equal to $\frac{\pi}{2}$, and the $\mathbb{T}$-tensor in Eq. (2) is computed by integrating the tensor $\mathbb{T}(\theta, \varphi)$ such that

$$\mathbb{T}_{vert} = \int_{\varphi=0}^{2\pi} \mathbb{T}(\theta, \varphi) \frac{\sin\theta}{4\pi} \, d\varphi \Big|_{\theta=\frac{\pi}{2}}. \quad (6)$$

The elastic modulus in loading direction reads as

$$\frac{1}{E_{dam,vert}} = \frac{1}{E}, \quad (7)$$

and Poisson's ratio as

$$\nu_{dam,vert} = \nu. \quad (8)$$

Thus, flat cracks running in loading direction do not damage the material's stiffness in that direction. This implies that non-vanishing aspect ratios are needed to model damage resulting from axisymmetric crack networks.

3.3 Non-Vanishing Aspect Ratios

Cracks with non-vanishing aspect ratios refer to $X \neq 0$, yielding a non-vanishing volume fraction of cracks. Thus, the damaged stiffness of concrete is now found as

$$\mathbb{C}_{dam} = f_c \mathbb{C}_c : \left[f_c \mathbb{I} + \frac{4\pi}{3} \omega \mathbb{T}_{vert} \right]^{-1}, \quad (9)$$

where f_c denotes the volume fraction of uncracked concrete. It is related to the volume fraction of the cracks as $f_c = 1 - f_{cr}$. The

relations between the elastic modulus of concrete and the crack density parameter, as well as between Poisson's ratio and the crack density parameter, for different values of the aspect ratio X, are shown in Figure 6 (a) and (b).
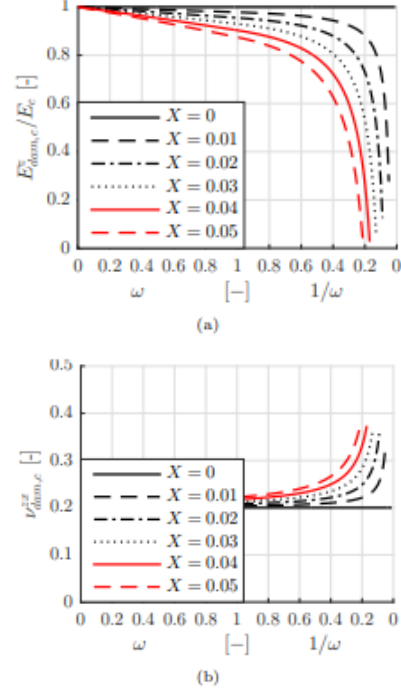
Figure 6: Relations between (a) elastic modulus, and (b) Poisson's ratio of concrete and ω for different aspect ratios in an axisymmetric crack orientation.

Figure 6 (a) and (b) show that micro-cracking with non-vanishing aspect ratios results in the *increase* in Poisson's ratio of damaged concrete. This is in qualitative agreement with experimental observations [15], showing an increase of ν right before compressive failure due to axial splitting.

3.4 Implications for modelling: Introduction of the damage factor γ

Rossi et al. [1] measured the number of cracks, N, created during the nonlinear creep test, but crack sizes and orientations could not be identified. This provides the motivation to introduce a damage factor γ such that the expression for the compliance of concrete damaged by diffuse microcracking takes the form

$$\frac{1}{E_{dam}} = \frac{1}{E} \left[1 + \frac{N}{V} \gamma^3 \right]. \quad (10)$$

with

$$\gamma^3 = a^3 f(\nu). \qquad (11)$$

In Eq. (11), a is a representative crack size and $f(\nu)$ refers to the influence of the unknown orientational properties of the crack network on the damage of concrete. Eq. (10) emphasizes that the creation of a new crack relates to a *linear* increase in the compliance of damaged concrete. Given that the crack sizes and orientations largely depend on the size, the mechanical properties, and the geometrical properties of the aggregates, as well as on the type of macroscopic loading, the value of the damage factor γ^3 must be identified for different tests.

4 MICROMECHANICS-INSPIRED APPROACH TO NONLINEAR CREEP

4.1 Linear viscoelasticity informed by crack micromechanics

Linear viscoelasticity relates to the use of the superposition principle, which in its uniaxial form is expressed as

$$\varepsilon = \int_{-\infty}^{t} J(t-\tau)\frac{d\sigma}{d\tau}d\tau, \qquad (12)$$

where ε is the strain, J is the uniaxial creep compliance, σ is the applied stress, t is the time variable resolving the strain measurements, and τ is the time variable resolving the stress history.

The viscoelastic response of the hierarchically organized material concrete is herein modelled in the framework of continuum micromechanics, see Figure 7. Boltzmann's superposition principle, see Eq. (12), can be solved for the case of creep of cracked concrete by transforming the time-dependent problem into the Laplace-Carson space, using the Mori-Tanaka scheme for penny-shaped cracks embedded in an undamaged concrete matrix, and back-transforming the results into the time domain. Accounting for the relations obtained in Section 3, see also [5], this can be written as

$$J_{dam}(t-\tau) = \left[1 + \frac{N(t)}{V}\gamma^3\right]J(t-\tau). \quad (13)$$
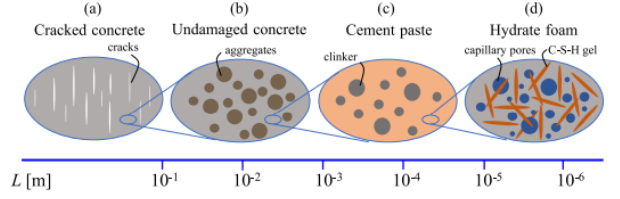
Figure 7: Qualitative properties of the hierarchically organized structure of concrete; 2D sketches of 3D RVEs of (a) damaged concrete, (b) undamaged concrete, (c) cement paste, and (d) hydrate foam; taken from [5].

4.2 Damage-dependent nonlinear creep

The nonlinear viscoelastic response of damaged concrete is herein described using a power-law function for linear creep, in combination with (i) a creep reduction factor accounting for different levels of time-invariant relative humidity, (ii) the affinity parameter [2] accounting for nonlinear viscoelasticity, and (iii) the new damage factor. This leads to

$$J_{dam}(t-\tau) = \left[1 + \frac{N}{V}\gamma^3\right]\left\{\frac{1}{E} + \frac{\eta\,RH}{E_c}\left[\frac{t-\tau}{t_{ref}}\right]^{\beta}\right\},$$
$$(14)$$

where E is the elastic modulus of uncracked concrete, E_c and β are its creep modulus and the creep exponent modulus of uncracked concrete quantified according to the micromechanics model of [16,17], $t_{ref} = 1$ day is a reference time, RH is the reduction factor accounting for relative humidity, see Figure 8, and η is the affinity parameter which is a function of the stress-to-strength ratio, σ/σ_{ult}, as

$$\eta = 1 + 2\left[\frac{\sigma}{\sigma_{ult}}\right]^4. \qquad (15)$$
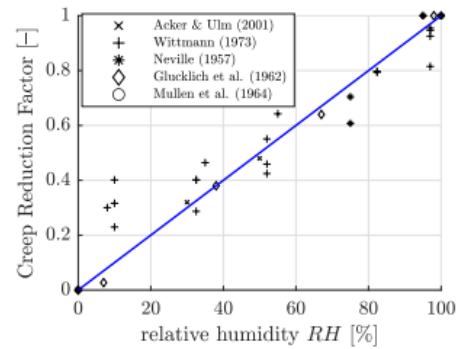
Figure 8: Creep reduction factor as a function of the internal relative humidity of concrete; after [5].

For multilevel nonlinear creep tests, an extension of the superposition principle was proposed by [18], which for the present model is written as

$$\varepsilon(t) = \left[1 + \frac{N}{V}\gamma^3\right]\left\{\frac{\sigma(t)}{E} + \sum_{i=1}^{n}[\sigma_i\,\eta_i - \right.$$

$$\left. \sigma_{i-1}\eta_{i-1}]\frac{\eta\,RH}{E_c}\left[\frac{t-t_i}{t_{ref}}\right]^{\beta}H(t-t_i)\right\}, \quad (16)$$

where H refers to the Heaviside function. Remarkably, all the coefficients in Eq. (16) are known based on the measured data as well as the micromechanical models [16,17], except for the damage factor γ. It is identified in the following.

4.3 Identification of the damage factor in the multistage creep test by Rossi et al. [1]

The damage factor is identified such that Eq. (16) best reproduces the measured data. Given that the mechanical properties at the age of 266 days, when the test started, are unknown (properties were only tested at an age of 28 days), three different sets of mechanical properties were considered, denoted by the index $k = 1, 2, 3$. The optimized damage factors obtained were $\gamma_1 = 11.7$ mm, $\gamma_2 = 12.7$ mm, $\gamma_3 = 13.6$ mm, see Figure 9.
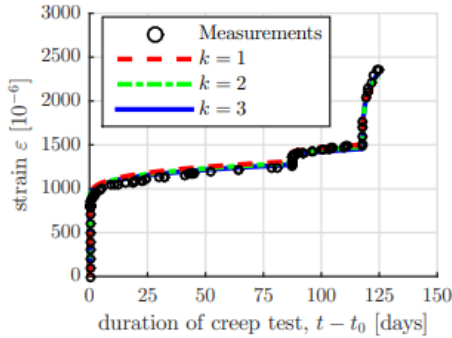
Figure 9: Comparison between the developed model and the measured strain; $k = 1, 2, 3$ refers to the uncertainty regarding the strength of the tested concrete; taken from [5].

5 MICROCRACK CREATION DURING CREEP TESTS

A key input for the development of the model is the history of acoustic emissions. It was measured during the simulated tests but is rarely available for other creep tests. Thus,

evolution laws for the creation of microcracks [5] are herein reported such that the model may be applied to and validated with additional creep tests in which the creation of cracks was not measured.

For this purpose, two types of diffusely created microcracks are identified: microcracks created during short-term loading due to an increase in the stress, denoted as N_σ, and microcracks created during sustained loading due to progressive creep deformation, denoted as N_ε. Together, they make up the total number of cracks as

$$N = N_\sigma + N_\varepsilon. \quad (17)$$

5.1 Microcracks created during quasi-instantaneous load application

The relation between the accumulated number of microcracks created during quasi-instantaneous load application and the stress-to-strength ratio is obtained by a power-law, see also [5], as

$$N_\sigma = \pi_a\left[\frac{\sigma}{\sigma_{ult}}\right]^{\pi_b}, \quad (18)$$

where π_a and π_b were optimized for each set of mechanical properties (see index $k = 1, 2, 3$), as $\pi_a = 2021$ and $\pi_b = 3$ for $k = 1$; $\pi_a = 2240$ and $\pi_b = 3$ for $k = 2$; and $\pi_a = 2474$ and $\pi_b = 3$ for $k = 3$, see Figure 10.
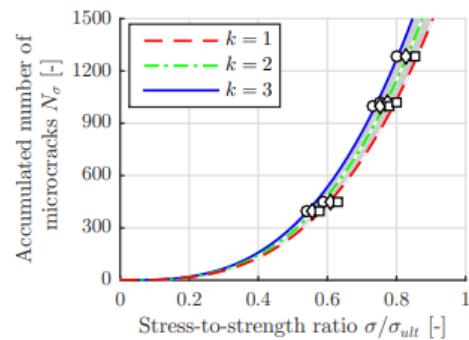
Figure 10: Accumulated number of microcracks during quasi-instantaneous load application; taken from [5].

5.2 Microcracks created during sustained loading

During each phase of sustained loading, the number of created microcracks increased almost linearly with the increasing creep strain, with a proportionality factor that increased with increasing stress-to-strength ratio, see also [5]. This is expressed as

$$N(t) - N(t_i^+) = \alpha_i \left(\frac{\sigma}{\sigma_{ult}}\right) \times [\varepsilon(t) - \varepsilon(t_i^+)], \tag{19}$$

where t_i^+ refers to the time instant at the beginning of each load step, right after the application of the load. The relation between α_i and the stress-to-strength ratio was modeled as a piecewise linear function. Every piece is expressed as

$$\alpha = \pi_c \left[\frac{\sigma}{\sigma_{ult}}\right] + \pi_d, \tag{20}$$

where π_c and π_d were optimized independently for three intervals of the stress-to-strength ratio, namely (a) $\frac{\sigma}{\sigma_{ult}} \leq \left(\frac{\sigma}{\sigma_{ult}}\right)_I$; (b) $\left(\frac{\sigma}{\sigma_{ult}}\right)_I \leq \frac{\sigma}{\sigma_{ult}} \leq \left(\frac{\sigma}{\sigma_{ult}}\right)_{II}$, referring to the limit of applicability of the affinity concept; and (c) $\frac{\sigma}{\sigma_{ult}} > \left(\frac{\sigma}{\sigma_{ult}}\right)_{II}$, referring to values beyond the limit of applicability of the affinity concept, see also [5]. The optimized values of π_c, π_d, $\left(\frac{\sigma}{\sigma_{ult}}\right)_I$, and $\left(\frac{\sigma}{\sigma_{ult}}\right)_{II}$ also depend on the set of mechanical properties, $k = 1, 2, 3$, as:

- For $k = 1$, $\left(\frac{\sigma}{\sigma_{ult}}\right)_I = 0.55$, $\left(\frac{\sigma}{\sigma_{ult}}\right)_{II} = 0.76$: $\pi_c = 0$ and $\pi_d = 0$ for interval (a), $\pi_c = 3.178 \times 10^6$ and $\pi_d = -1.739 \times 10^6$ for interval (b), and $\pi_c = 102.8 \times 10^6$ and $\pi_d = -77.01 \times 10^6$ for interval (c), see the red dashed line of Figure 11.

- For $k = 2$, $\left(\frac{\sigma}{\sigma_{ult}}\right)_I = 0.53$, $\left(\frac{\sigma}{\sigma_{ult}}\right)_{II} = 0.73$: $\pi_c = 0$ and $\pi_d = 0$ for interval (a), $\pi_c = 3.289 \times 10^6$ and $\pi_d = -1.739 \times 10^6$ for interval (b), and $\pi_c = 106.3 \times 10^6$ and $\pi_d = -77.01 \times 10^6$ for interval (c), see the green dashed-dotted line of Figure 11.

- For $k = 3$, $\left(\frac{\sigma}{\sigma_{ult}}\right)_I = 0.51$, $\left(\frac{\sigma}{\sigma_{ult}}\right)_{II} = 0.71$: $\pi_c = 0$ and $\pi_d = 0$ for interval (a), $\pi_c = 3.400 \times 10^6$ and $\pi_d = -1.739 \times 10^6$ for interval (b), and $\pi_c = 109.9 \times 10^6$ and $\pi_d = -77.01 \times 10^6$ for interval (c), see the blue solid line of Figure 11.
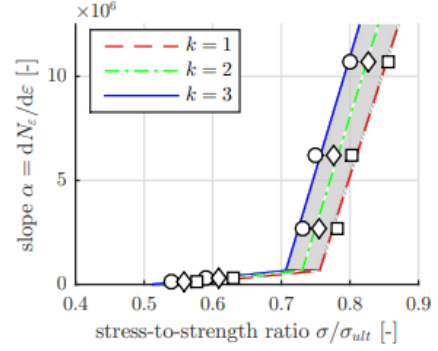
Figure 11: Relation between the slope α_i and the stress-to-strength ratio; taken from [5].

The number of cracks accumulated during the whole multistage creep test can then be calculated, see also [5], as

$$N_\varepsilon = \Delta N_i + \sum_{j=1}^{i-1} \Delta N_j \ , t_i^+ \leq t \leq t_{i+1}^-, i > 1. \tag{21}$$

6 MODEL VALIDATION

The developed nonlinear creep model was validated in [5] by predicting the strain evolution of two independent tests on concrete of the same composition as that tested by Rossi et al. [1], see [19], as well as by simulating and identifying the damage factor for two tests by Kammouna et al. [20]. In the following two subsections, two further sets of tests are analyzed.

6.1 Tests on CEM I Concrete

Herein, the tests by Ranaivamonana et al. [21] are analyzed. A sensitivity analysis regarding uncertainties on the strength of concrete at the time of testing was performed, yielding three sets of mechanical properties $k = 1, 2, 3$. The mechanical properties obtained

using the micromechanical model were then as follows:

- For $k = 1$, $\sigma_{ult} = 61.6$ MPa, $E = 42.1$ GPa, $E_c = 278.2$ GPa, $\beta = 0.25$. The damage factor was then optimized as $\gamma = 7.0$ mm, see the red dashed curve in Figure 12.
- For $k = 2$, $\sigma_{ult} = 64.6$ MPa, $E = 42.6$ GPa, $E_c = 286.7$ GPa, $\beta = 0.25$. The damage factor was then optimized as $\gamma = 7.4$ mm, see the green dashed-dotted curve Figure 12.
- For $k = 3$, $\sigma_{ult} = 67.7$ MPa, $E = 43.1$ GPa, $E_c = 294.4$ GPa, $\beta = 0.25$. The damage factor was then optimized as $\gamma = 7.6$ mm, see the blue solid curve in Figure 12.
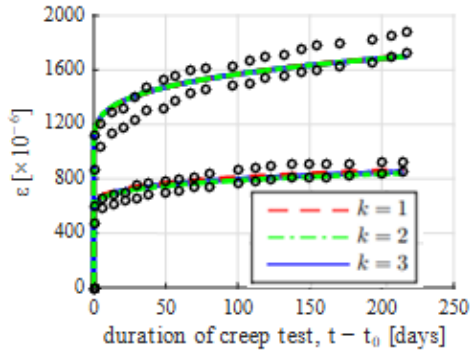
Figure 12: Simulation of the compressive strain evolution in the single-step tests on CEM I concrete by Ranaivomanana et al. [21]: the red, green, and blue graphs refer to k = 1, 2, and 3, respectively.

The results shown in Figure 12 underline that the described model is capable of simulating the tests of Ranaivomanana et al. [21] accurately. The first test, at a low stress-to-strength ratio, refers to linear creep, and serves to check the validity of the micromechanical model. The second test, at a moderately large stress-to-strength ratio, refers to a nonlinear viscoelastic test, and checks the validity of the affinity concept.

6.2 Tests on CEM II Concrete

Herein, the tests by Dummer et al. [22] are analyzed. The reported mean and standard deviations of a set of measurements are compared with simulations of the individual tests (several curves of Figure 13 refer to one

mean and standard deviation). The elastic modulus of uncracked concrete was measured at the time of testing: $E = 30.3$ GPa. The creep modulus was determined in [11]: $E_c = 103.1$ GPa. In addition, $\beta = 0.25$. Uncertainties refer to the strength of concrete:

- For $k = 1$, $\sigma_{ult} = 29.7$ MPa, and the optimal damage factor is quantified as $\gamma = 8.4$ mm, see the red dashed curve in Figure 13.
- For $k = 2$, $\sigma_{ult} = 31.8$ MPa, and the optimal damage factor is quantified as $\gamma = 9.2$ mm, see the green dashed-dotted curve in Figure 13.
- For $k = 3$, $\sigma_{ult} = 33.9$ MPa, and the optimal damage factor is quantified as $\gamma = 10.1$ mm, see the blue solid curve in Figure 13.
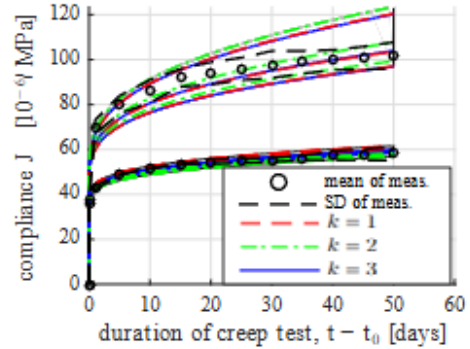
Figure 13: Simulation of the compressive strain evolution in the single-step tests on CEM II concrete by Dummer et al. [22]: the red, green, and blue graphs refer to k = 1, 2, and 3, respectively.

The first set of tests, at low stress-to-strength ratios, serves to check whether the linear model is accurate. The second set of tests, at high stress-to-strength ratios, serves to validate the damage factor and the model proposed. The results confirm that the model may be applicable even to CEM II concretes, and provide motivation to verify, as an outlook, the applicability of the model also on concretes made up of other types of supplementary cementitious materials, see e.g. [23].

7 CONCLUSIONS

- The proposed model was successfully validated with sets of tests on CEM I and CEM II concretes at low, moderate,

8

and high stress-to-strength ratios.

- The number of cracks created are directly proportional to damage of concrete and linearly increase the compliance of concrete.
- The value of the damage factor is independent of the applied stress-to-strength ratio, as long as diffuse microcracking is realistic, and large cracks have not yet propagated.
- The origin of nonlinear creep is herein related to nonlinear viscoelastic phenomena, dominating at low and moderate stress levels, combined with microcracking-induced damage, governing the increase of deformation at large stress levels.

REFERENCES

[1] Rossi, P., Tailhan, J. L., Le Maou, F., Gaillet, L., & Martin, E. (2012). Basic creep behavior of concretes investigation of the physical mechanisms by using acoustic emission. *Cement and Concrete Research*, *42*(1), 61-73.

[2] Ruiz, M. F., Muttoni, A., & Gambarova, P. G. (2007). Relationship between nonlinear creep and cracking of concrete under uniaxial compression. *Journal of Advanced Concrete Technology*, *5*(3), 383-393.

[3] Bažant, Z. P., Hauggaard, A. B., Baweja, S., & Ulm, F. J. (1997). Microprestress-solidification theory for concrete creep. I: Aging and drying effects. *Journal of Engineering Mechanics*, *123*(11), 1188-1194.

[4] Bažant, Z. P., & Jirásek, M. (2018). *Creep and hygrothermal effects in concrete structures* (Vol. 225). Dordrecht, The Netherlands: Springer.

[5] Díaz Flores, R., Hellmich, C., & Pichler, B. (2025). Nonlinear creep of concrete: stress-activated stick-slip transition of viscous interfaces and microcracking-induced damage. Under re-revision at *Cement and Concrete Research*.

[6] Scheiner, S., & Hellmich, C. (2009). Continuum microviscoelasticity model for aging basic creep of early-age concrete. *Journal of Engineering Mechanics*, *135*(4), 307-323.

[7] Pickett, G. (1942, February). The effect of change in moisture-content on the crepe of concrete under a sustained load. In *Journal Proceedings* (Vol. 38, pp. 333-356).

[8] Binder, E., Königsberger, M., Flores, R. D., Mang, H. A., Hellmich, C., & Pichler, B. L. (2023). Thermally activated viscoelasticity of cement paste: minute-long creep tests and micromechanical link to molecular properties. *Cement and Concrete Research*, *163*, 107014.

[9] Shahidi, M., Pichler, B., & Hellmich, C. (2016). Interfacial micromechanics assessment of classical rheological models. I: Single interface size and viscosity. *Journal of Engineering Mechanics*, *142*(3), 04015092.

[10] Shahidi, M., B. Pichler, and Ch Hellmich. Interfacial micromechanics assessment of classical rheological models. II: Multiple interface sizes and viscosities. *Journal of Engineering Mechanics* 142.3 (2016): 04015093.

[11] Sorgner, M., Díaz Flores, R., Pichler, B., Pilgerstorfer, T., Moritz, B., & Hellmich, C. (2025). Basic creep properties of hydrates in mature slag-based CEM II concretes: A micromechanical analysis. *Cement and Concrete Research*, *189*, 107735.

[12] Budiansky, B., & O'Connell, R. J. (1976). Elastic moduli of a cracked solid. *International Journal of Solids and Structures*, *12*(2), 81-97.

[13] Benveniste, Y. (1987). A new approach to the application of Mori-Tanaka's theory in composite materials. *Mechanics of Materials*, *6*(2), 147-157.

[14] Dormieux, L., Kondo, D., & Ulm, F. J. (2006). *Microporomechanics*. John Wiley & Sons.

[15] Mazzotti, C., & Savoia, M. (2003). Nonlinear creep damage model for concrete under uniaxial compression. *Journal of Engineering Mechanics*, *129*(9), 1065-1075.

[16] Königsberger, M., Irfan-ul-Hassan, M.,

Pichler, B., & Hellmich, C. (2016). Downscaling based identification of nonaging power-law creep of cement hydrates. *Journal of Engineering Mechanics*, *142*(12), 04016106.

[17] Irfan-ul-Hassan, M., Königsberger, M., Reihsner, R., Hellmich, C., & Pichler, B. (2017). How water-aggregate interactions affect concrete creep: Multiscale analysis. *Journal of Nanomechanics and Micromechanics*, *7*(4), 04017019.

[18] Tasevski, D., Ruiz, M. F., & Muttoni, A. (2018). Compressive strength and deformation capacity of concrete under sustained loading and low stress rates. *Journal of Advanced Concrete Technology*, *16*(8), 396-415.

[19] Rossi, P., Tailhan, J. L., & Le Maou, F. (2013). Creep strain versus residual strain of a concrete loaded under various levels of compressive stress. *Cement and Concrete Research*, *51*, 32-37.

[20] Kammouna, Z., Briffaut, M., & Malecot, Y. (2019). Experimental study of the creep effect on the mechanical properties of concrete. *Advances in Civil Engineering*, *2019*(1), 5907923.

[21] Ranaivomanana, N., Multon, S., & Turatsinze, A. (2013). Tensile, compressive and flexural basic creep of concrete at different stress levels. *Cement and Concrete Research*, *52*, 1-10.

[22] Dummer, A., Smaniotto, S., & Hofstetter, G. (2023). Experimental and numerical study on nonlinear basic and drying creep of normal strength concrete under uniaxial compression. *Construction and Building Materials*, *362*, 129726.

[23] Schmid, S. J., Zelaya-Lainez, L., Lahayne, O., Peyerl, M., & Pichler, B. (2025). Hourly three-minute creep testing of an LC3 paste at early ages: Advanced test evaluation and the effects of the pozzolanic reaction on shrinkage, elastic stiffness, and creep. *Cement and Concrete Research, 187,* 107705.